Numerical microstructure model of NiTi wire reconstructed from 3D-XRD data

L Heller[1,2], I Karafiatova [3], L Petrich[4], Z Pawlas[3], P Shayanfard[1], V Beneš [3], V Schmidt[4] and P Šittner[1,2]

[1] Institute of Physics of the Czech Academy of Sciences, Na Slovance 2,182 21 Prague, Czech Republic

[2] Nuclear Physics Institute of the Czech Academy of Sciences, Husinec - Řež, čp. 130, 250 68 Řež, Czech Republic

[3] Department of Probability and Mathematical Statistics, Faculty of Mathematics and Physics, Charles University, Sokolovská 83, 186 75 Prague, Czech Republic

[4] Institute of Stochastics, Faculty of Mathematics and Economics, Ulm University, 89069 Ulm, Germany

E-mail: `heller@fzu.cz`

Abstract. In this paper, the grain microstructure and strain partitioning in a polycrystalline NiTi wire subjected to tensile loading was reconstructed from an experimental 3D-XRD dataset. The reconstruction of a volume containing more than 8,000 stressed grains involved optimization with respect to both the geometrical features and material elastic properties. The geometrical features of the microstructure were reconstructed using Laguerre tessellations based on the experimental 3D-XRD dataset. Two different algorithms fitting Laguerre tessellations were applied in order to assess the sensitivity of the reconstruction to the choice of the algorithm. The material properties in terms of elastic anisotropy were refined from an initial published value to minimize the mismatch between experiment and simulation using an optimization algorithm based on linear elasticity simulations. As a result of this, we constructed a numerical microstructure model that statistically matches the experimentally probed material in terms of positions and sizes of grains as well as partitioning of elastic strain and stress in the microstructure (average elastic properties and standard deviations of piecewise constant components of elastic strain and stress tensors in grains).

Keywords: elastic anisotropy, elasticity, microstructure, microstructure reconstruction, 3D-XRD, Laguerre tessellation, FEM

Submitted to: *Modelling Simul. Mater. Sci. Eng.*

1. Introduction

Realistic microstructure models are essential for representative modeling of deformation phenomena in polycrystals on the level of individual grains and their interactions. In general, a realistic microstructure model of a single-phase material has to accurately represent the microstructure morphology, and be accurately informed of crystal orientations and material parameters characterizing crystal symmetry and deformation behavior of single grains. 3D synchrotron x-ray diffraction (3D-XRD) [1] applied to a statistically significant number of grains (detector configuration C in [1]), hereinafter referred to as 3D-XRD method or 3D-XRD, provides many of these elements necessary to build microstructure models. Namely, it provides information on microstructure geometry in terms of grain center-of-mass positions, grain volumes, and grain orientations. Furthermore, 3D-XRD may provide information on elastic deformation of grains in terms of grain-wise averaged elastic strains. Nevertheless, 3D-XRD does not provide information on grain shapes, grain boundaries, grains' neighborhoods, and inhomogeneity of strain and stress fields within individual grains due to interactions of anisotropically deforming grains. This missing information may be extracted from numerical simulations performed on microstructure models provided that these models accurately represent real microstructures and the elastic constitutive response of the material.

The morphology of the microstructures has been modeled using Voronoi [2] and Laguerre tessellations [3], where the grains are approximated by convex polyhedral cells [4], hereinafter interchangeably referred to as grains or cells. Laguerre tessellations enable to optimize the cells geometry and position on provided geometrical statistics such as grain size distributions or grain-wise input data such as grain sizes and center-of-mass positions as experimentally identified by e.g. 3D-XRD [1], 3D-EBSD [5]. It has been reported in the literature that Laguerre tessellations perform well in reproducing statistics of real microstructures, but they are not as accurate in reproducing the topology of individual grains and relationships between grains [6]. However, the accuracy of the latter was shown to be improved by using more sophisticated optimization methods coupled with Laguerre tessellations [7, 8, 9].

To sum up, the tessellation-based polycrystal models have been used to study various deformation mechanisms activated in deformed metals such as elasticity, dislocation plasticity, deformation twinning, displacive phase transformation and their coupling [10, 11, 12, 13, 14]. However, these models have never been proven to represent accurately the deformation behavior of real microstructures. The validation of Laguerre-tessellation-based microstructure models has been performed strictly on morphological comparisons between experimentally probed microstructures and their representations by tessellations [6, 7, 8, 9]. Perfect grain to grain match between statistically significant polycrystal models and real microstructures cannot be reached due to limitations of both experimental techniques and the mathematical framework of Laguerre tessellations. Nevertheless, statistically equivalent microstructure models comprising thousands of grains can be reconstructed from experimental data. Although essential for reliabil-

ity of simulations performed on statistically equivalent tessellation models, the critical validation of these models in terms of statistical descriptors of deformation behavior remains rare in the literature.

The aim of this paper is twofold. First, a microstructure model of NiTi reconstructed from experimental data is aimed for further through-simulation understanding of stress-induced martensitic transformation (MT) on the mesoscopic level of polycrystalline aggregates. Due to stress-induced MT and coupled deformation processes the superelastic NiTi wires exhibit outstanding structural and functional properties [15, 16, 17, 18] the application of which is, however, largely hindered by poor fatigue performance in the superelastic regime [19, 20]. The fatigue problems might stem from local stress inhomogeneity due to grain interactions and redistribution of stresses activated by anisotropy of deformation processes proceeding in NiTi wires under stress [18, 21, 22, 23]. These phenomena have been studied on the surface [24] but are difficult to be studied in the bulk. Mesoscopic simulations can be used instead of experiments provided that the microstructure model accurately represents the real microstructure. The verification of this assumption is the second aim of the present paper.

The verification is based on statistical comparisons between the 3D-XRD experiment and the microstructure model in terms of morphology and deformation behavior. The latter relies on comparisons of grain-wise averaged strain and stress distributions resulting from elastic deformation. In fact, such validation based on deformation behavior is an overall test of the model as the deformation behavior reflects all model features such as morphological aspects, the distribution of grain orientations, and elastic properties. The single crystal elastic properties of phase transforming shape memory alloys have, however, been often reported as changing prior to phase transformation. Pretransformation softening has been experimentally observed during both temperature-induced and stress-induced MT [25, 26, 27]. The reconstruction of the microstructure model presented in this paper takes this phenomenon into account by refining the elastic anisotropy from the value determined by initial elastic constants identified in stress-free conditions well above the phase transformation temperature. The refinement is based on the match between 3D-XRD and simulation results in terms of elastic anisotropy-driven scatter in grain-wise averaged strain components. In this paper we report a considerable mismatch regarding this measure for the initial elastic constants, being an indirect evidence for changes in elastic constants prior to stress-induced MT in NiTi. Note that the mismatch might also stem from any plastic deformation. Although we cannot fully rule out an occurrence of microplasticity, we can exclude any considerable plastic deformation. In fact, we have investigated thoroughly plastic deformation phenomena in the superelastic NiTi wires with respect to microstructure, temperature and deformation regime, i.e., prior, during, and after the stress-induced MT [23, 18]. The major conclusion is that the yield stresses of austenite and martensite lie well above the superelastic stress-plateau at room temperature, i.e., above the stress level applied in the present case. In-situ X-ray powder diffraction experiments as well as the 3D-XRD experiments did not reveal any distortion of diffraction peaks nor spots indicating the plastic deformation. Moreover,

no any residual macroscopic strain was induced by tensile loading up to the level of the stress-plateau and unloading that followed a reversible linear elastic stress-strain trend. The paper includes three main sections dedicated to the presentation of the experimental 3D-XRD dataset the microstructure model is based on, the description of the applied methods, and the results. Section 3 entitled "Methods" includes subsections dealing with the reconstruction of microstructure morphology using Laguerre tessellations and two different optimization schemes, finite element modeling to simulate the deformation behavior, and a description of the elastic anisotropy refinement. Section 4 entitled "Results" describes the match between the experimental 3D-XRD dataset and the models in terms of morphological aspects, and the deformation behavior for the initial and refined anisotropies. Finally, the main results of the present paper are discussed and concluded in Sections 5 and 6, respectively.

2. Experimental dataset

The present paper is based on a 3D-XRD experiment originally focused on the evaluation of stress redistribution near the martensite shear band front (MSBF) propagating under tension in 100 μm superelastic NiTi wire [21]. As schematically shown in Fig. 1b, the MSBF propagates upon tensile loading throughout the wire at a constant stress indicated by the plateau in the stress-strain loading curve (Fig. 1a). At MSBF the cubic B2 austenite transforms into monoclinic B19' martensite, which provides the wire with $\sim$ 8% of reversible tensile deformation. The grains transformed into martensite could not be probed by 3D-XRD due to overlap and diffuseness of the diffraction spots caused by twelve possibly formed martensite orientation variants and transformation induced plasticity. Therefore, the 3D-XRD method probed $\sim$ 15,000 austenitic grains near the MSBF (Fig. 1c) where the lattice orientation, volume and average elastic strain tensor were identified for individual grains. The distribution of grain-wise averaged axial strains showed that the conical MSBF affects the stress state in grains located in its vicinity spanning up to $\sim$ 100μm from the cone tip as illustrated in Fig. 1d (for details we refer to [21]). However, beyond this region the grains are left unaffected by MSBF and their stress-strain state can be considered as purely due to elastic grain interactions induced by tensile loading. This region (dash-dotted in Fig. 1d) represents the volume of interest for the present paper and will be hereinafter referred to as the wire microstructure. It contains 8,063 grains constituting the wire microstructure to be reconstructed in the present paper while the experimental 3D-XRD data informing about this microstructure will be hereinafter referred to as 3D-XRD dataset.

The 3D-XRD dataset provides information about the wire microstructure features in terms of center-of-mass positions, volume and crystal lattice orientation of individual grains and about elastic grain interactions in terms of grain-wise averaged strain tensor components. The former provides a basis for the reconstruction of microstructure morphology while the latter serves for the refinement of elastic anisotropy and for the

validation of the microstructure model. Note that the 3D-XRD dataset is defined in a laboratory coordinate system the z-axis of which is aligned with the wire axis as seen in Fig. 1c,d.

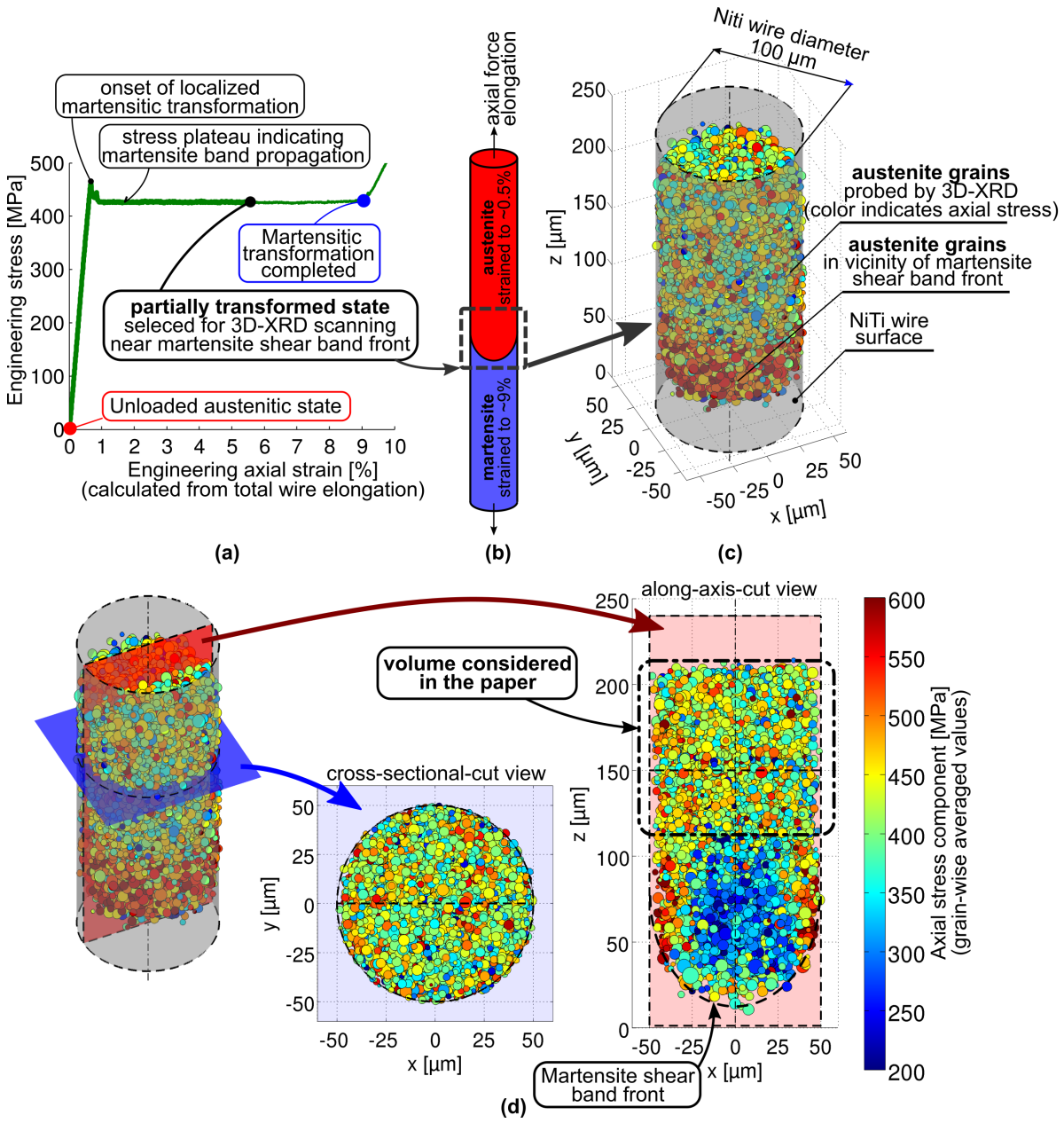

Figure 1. The present paper is based on a 3D-XRD measurement of a NiTi wire being under tension in a partially transformed state manifested macroscopically by the stress plateau in the stress-strain curve (a) and the loading stage in the middle of the stress plateau. The 3D-XRD measurement probed a vicinity of the martensite shear band front (b), and provided information on individual austenite grains in terms of lattice orientation, volume, and tensorial strains (c). A set of austenitic grains that remained unaffected by the martensite shear band front (dash-dotted region in (d)) was considered for microstructure reconstruction in this paper.

2.1. Microstructure

The 3D-XRD dataset reveals that the wire microstructure features a log-normal distribution of grain volumes with mean value and standard deviation (std) of 62 and 2 μm^3, respectively (Fig. 2a), and normal distribution of volume-equivalent grain diameters with mean value and std of 5.1 and 1.3 μm, respectively (Fig. 2b). The grain shape morphology was qualitatively evaluated as equiaxial based on the 3D EBSD analysis reported in [21].

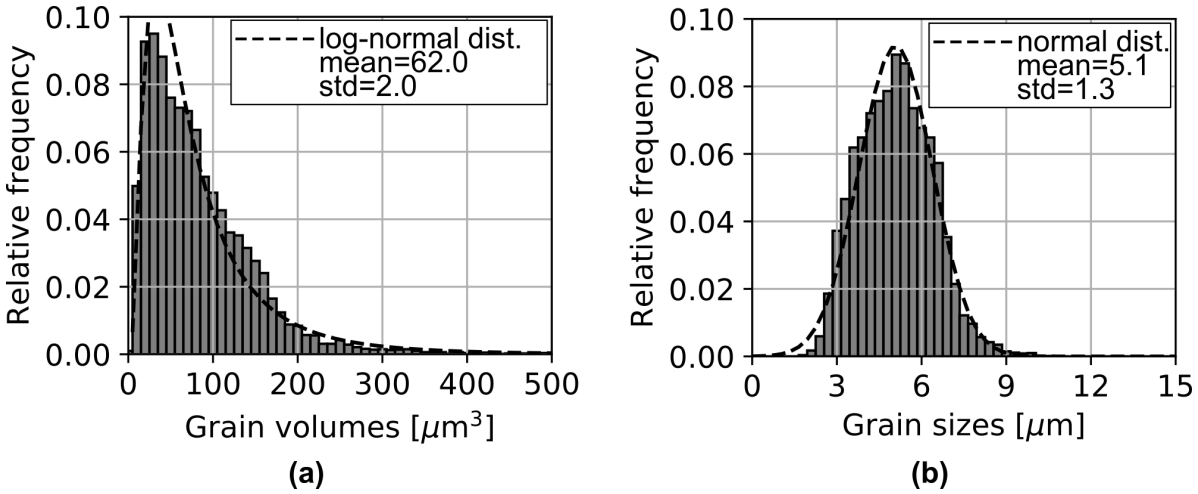

Figure 2. Distribution of grain volumes (a), and volume-equivalent grain diameters (b) of the wire microstructure as identified by the 3D-XRD method and approximated by a log-normal distribution and a normal distribution, respectively.

The 3D-XRD dataset provides complete crystallographic information about the lattice orientation of individual grains , e.g., in terms of three Euler angles. The preferential crystallographic orientation of the microstructure (texture) was assessed using pole figures evaluated in the laboratory coordinate system where the z-axis is aligned with the wire axis and the x,y-axes lie in the wire cross-section. The pole figure for <111> directions (Fig. 3a) reveals their strong preferential orientation along the wire axis and the <100> pole figure (Fig. 3b) confirms the strong fiber texture of the microstructure.

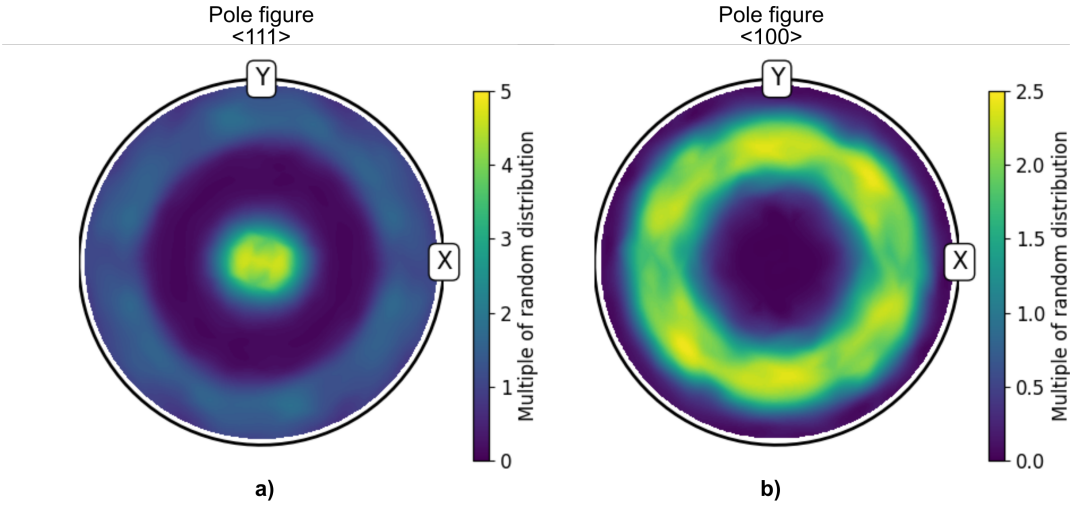

Figure 3. Preferential grain orientations of the wire microstructure expressed in terms of the <111> pole figure (a) and the <100> pole figure (b) plotted in equal area projection in the laboratory coordinate system where the z-axis is aligned with the wire axis and the x,y-axes lie in the wire cross-section.

2.2. Distribution of grain-wise averaged strains

The 3D-XRD dataset provides information about the elastic strains within the polycrystalline aggregate in terms of grain-wise averaged strain tensor components that were identified using the 3D-XRD method with experimental errors estimated to be about 1e-4 (for details see the supplementary material of [21]).
Unweighted distributions of grain-wise averaged strains with indicated mean and standard deviation values are presented in Fig. 4 for all independent components of the strain tensor expressed in the laboratory coordinate system, where the xy-plane lies in the wire cross-section plane. Moreover, the inset figure informs about relative azimuthal variations of radial and hoop strains (Fig. 4b), and the radial Poisson ratio (Fig. 4c) evaluated within the wire cross-section. The azimuthal variations were evaluated relatively to their average values over the full azimuthal range. The azimuthal variations being lower than 1.0 % confirms that the assumption of axial symmetry holds reasonably well.

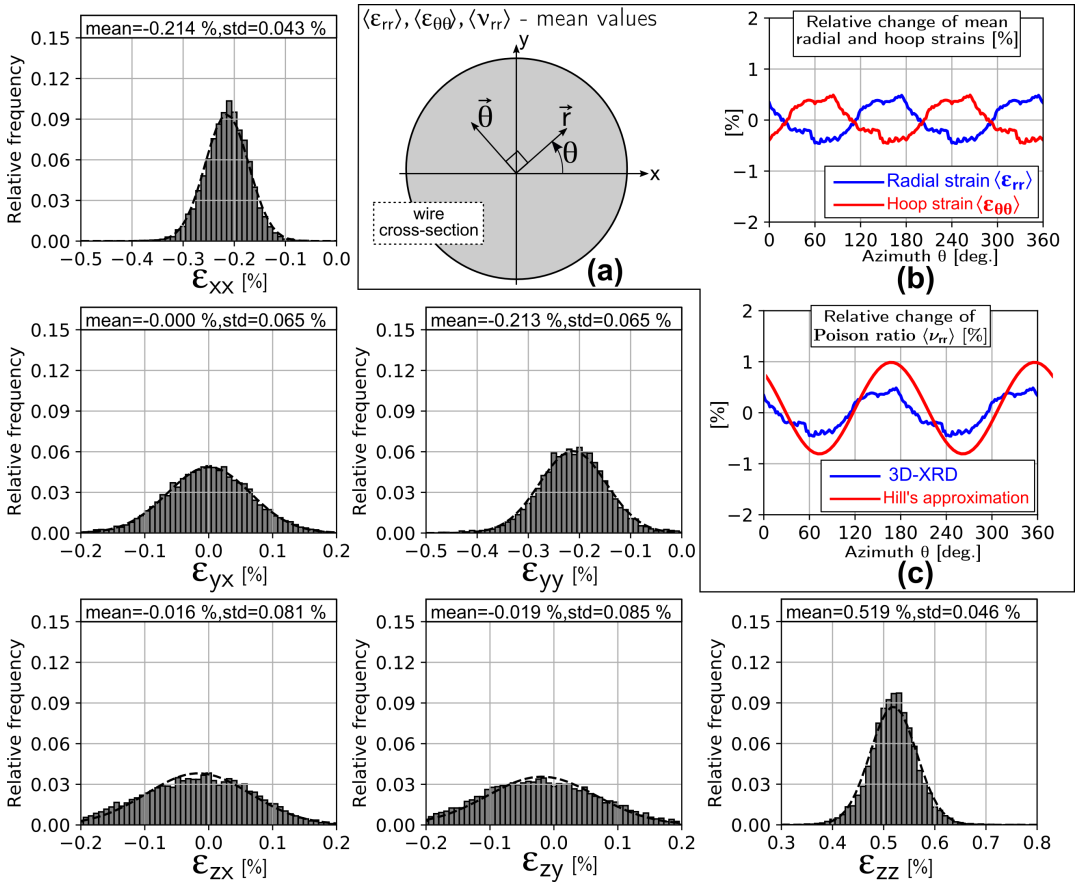

Figure 4. Histograms fitted by normal density functions with indicated mean and standard deviation (std) values representing unweighted distributions of grain-wise averaged strains for all independent components of strain tensors expressed in the laboratory coordinate system, where the z-axis is aligned with the wire axis while the xy-plane lies in the wire cross-section plane as indicated by the inset figure (a). The inset plots (b) and (c) show the relative azimuthal variations of mean values of radial and hoop strains, and the radial Poisson ratio within the cross-section plane depicted in (a), respectively.

3. Methods

3.1. Reconstruction of microstructure morphology

The morphology of the microstructure model to be constructed in the present paper was based on Laguerre tessellations (see, e.g., [3]) that were optimized such that each cell matches the corresponding grain in the 3D-XRD dataset as closely as possible in terms of grain size and center-of-mass position. Two different models were considered, each of them using a different reconstruction algorithm in order to assess how the reconstruction method affects the resulting microstructure morphology and simulated elastic grain interactions. One of the two algorithms described briefly hereinafter has been developed in [7] by co-authors of the present paper, referred to as CE (cross-entropy) method, while the second one has been developed in [8, 9] and implemented in the open-source software

package Neper by R. Quey (referred to as Neper).

3.1.1. Laguerre tessellations A Laguerre tessellation is completely described by a $4n$-dimensional vector where n denotes the number of cells. More precisely, each cell C_i of the tessellation ($i = 1, \ldots, n$) can be associated with a so-called generator consisting of a point $x_i \in \mathbb{R}^3$ and a weight $r_i \geq 0$. The cell C_i is then given by

$$C_i = \{y \in \mathbb{R}^3 : \mathrm{pow}(y, (x_i, r_i)) \leq \mathrm{pow}(y, (x_j, r_j)) \text{ for each } j = 1, \ldots, n\}$$

with $\mathrm{pow}(y, (x, r)) = ||y - x||^2 - r^2$. So the problem of reconstructing the wire microstructure morphology from the 3D-XRD dataset can be phrased as the optimization problem of finding the generators that minimize the discrepancy between volumes and centers of mass of the Laguerre cells and the grain sizes and centers of mass from the 3D-XRD dataset. The biggest differences of the two reconstruction methods described below are how exactly they measure this discrepancy, i.e., how the cost function is defined, and which optimization algorithms they employ.

3.1.2. CE method The method developed in [7] is based on cross-entropy optimization [28], where in each iteration of the algorithm several Laguerre tessellations (more precisely their generators) are drawn from some probability distribution. The best tessellations are selected with respect to the cost function and their generators are used to update the probability distribution for the next iteration. The benefits of this algorithm are that it does not easily get stuck in local minima and that the computations can be performed in a highly parallel and even distributed environment.

3.1.3. Neper method The reconstruction method proposed in [8], on the other hand, can employ several different non-linear, gradient-free optimization algorithms. The unique feature, however, is that in each iteration of the reconstruction only few generators are altered. In a Laguerre tessellation, these changes may also affect neighboring cells and, in order to make the program more efficient, an update strategy of the cost function is used that propagates these changes through the tessellation and only the costs of the modified cells are recomputed.

3.2. Numerical simulations

3.2.1. Finite element discretization and elastic anisotropy assignment Elastic grain interactions in the NiTi wire were simulated on microstructure models by the finite element method (FEM) using the structural static analysis of the MSC Marc solver [29]. The microstructure models were discretized using the Neper software allowing for regularization of tessellations and subsequent discretization of each individual cell by tetrahedral elements [9]. In order to verify the sensitivity of simulation results to the degree of discretization, two versions of finite element models were prepared one of which used linear four nodes tetrahedral elements (Element 134 [30]) while the other one used more accurate quadratic ten nodes tetrahedral elements (Element 127 [30]).

The anisotropy was assigned to sets of elements representing individual grains using the orientation option in conjunction with the 3D ANISO orientation type [31], where the grain orientation is defined by the basal lattice vectors expressed in the global coordinate system coinciding with the laboratory coordinate system of the 3D-XRD experiment. The vectors were calculated from grain orientations available in the 3D-XRD dataset. The elastic properties were then defined in the local coordinate systems by a single stiffness matrix filled with the considered elastic constants.

3.2.2. Boundary conditions The tensile loading in the NiTi wire was prescribed by boundary conditions defined in terms of axial stresses so to match as closely as possible the experimentally measured axial stresses in grains located at the boundaries. Therefore, the surfaces of grains located at the wire cross-sectional boundaries were subjected to axial stresses corresponding to grain-wise averaged axial stresses evaluated in these grains using the 3D-XRD measured lattice strains and considered elastic constants.

3.2.3. Post-processing of simulation results The match between the microstructure model and the real microstructure was evaluated by comparing the mean values and standard deviations of distributions of grain-wise averaged strain and stress components expressed in the laboratory cylindrical coordinate system having its z-axis aligned with the wire axis. This required an automated post-processing of the simulation results provided in terms of strains and stresses at the level of individual elements. Therefore, these results were reduced into grain-wise averaged strain and stress components denoted as $\varepsilon_{i,j}^{g,FEM}$, $\sigma_{i,j}^{g,FEM}$, respectively, by element-volume weighted averaging according to Eq. 1-2, where the superscript g denotes the indexes of individual grains and V^g denotes their volumes. The individual grains were discretized by N^g elements of volumes V_e^g on which the strain and stress components, denoted by $\sigma_{e,i,j}^{g,FEM}$, $\varepsilon_{e,i,j}^{g,FEM}$, were respectively evaluated as average values of stress and strain components calculated at the four vertices of the individual tetrahedral elements. The average values were computed with the help of the Python interface of the MSC Marc post-processor [32] and using the following equations:

$$\varepsilon_{i,j}^{g,FEM} = \frac{1}{V^g}\sum_{e=1}^{N^g} V_e^g \varepsilon_{e,i,j}^{g,FEM} \quad (i,j=1,2,3), \text{ and} \tag{1}$$

$$\sigma_{i,j}^{g,FEM} = \frac{1}{V^g}\sum_{e=1}^{N_e^g} V_e^g \sigma_{e,i,j}^{g,FEM} \quad (i,j=1,2,3). \tag{2}$$

3.3. Refinement of elastic anisotropy

The elastic properties of the austenite cubic structure of the NiTi wire are described by three elastic constants C_{11}, C_{12}, C_{44} fully defining the fourth order elasticity tensor $C_{i,j,k,l}^{test}$, where the values of the indices i,j,k,l range from 1 to 3. Experimentally

identified values of elastic constants are available in the literature for stress-free austenite. However, the 3D-XRD dataset is obtained on stressed material near stress-induced martensitic transformation, which may lead to premartensitic softening of the basal plane shear modulus $C' = (C_{11} - C_{12})/2$ [26, 27]. This softening changes the elastic anisotropy defined for cubic materials as $A = C_{44}/C'$. The magnitude of elastic anisotropy affects the magnitude of strain and stress inhomogeneities in the polycrystalline material, which may be evaluated by standard deviations of grain-wise averaged strains and stresses. Therefore, we suggest a method of elastic anisotropy refinement based on numerical simulations performed on a set of elastic constant combinations selected in the vicinity of the values experimentally identified under stress-free conditions. The mismatch between the 3D-XRD dataset and the simulation results in terms of standard deviations of distributions of grain-wise averaged strains is then considered as a criterion for identifying the elastic anisotropy of the material under stress. Specifically, the sum of absolute differences in standard deviations $\mathrm{std}(\varepsilon^g_{i,j})$ of distributions of all tensorial components of grain-wise average strains $\varepsilon^g_{i,j}$ is considered as a measure of refinement quality according to the following equation:

$$\Delta\mathrm{std}(\varepsilon^g) = \sum_{i=1}^{3}\sum_{j=1}^{3} \left|\mathrm{std}(\varepsilon^g_{i,j})^{\text{3D-XRD}} - \mathrm{std}(\varepsilon^g_{i,j})^{\text{FEM}}\right| , \tag{3}$$

where the superscripts 3D-XRD and FEM denote the values resulting from 3D-XRD measurement and simulations, respectively. Besides, the L_1 norm was also considered as a measure of the mismatch between the 3D-XRD dataset and the simulation results evaluated as a sum of absolute differences between vectors of histograms of grain-wise averaged strains according to the following equations:

$$\Delta\mathrm{L}_1(\varepsilon^g) = \sum_{i=1}^{3}\sum_{j=1}^{3}\sum_{k=1}^{N_h} \left|\mathrm{h}^{\mathrm{k}}(\varepsilon^g_{i,j})^{\text{3D-XRD}} - \mathrm{h}^{\mathrm{k}}(\varepsilon^g_{i,j})^{\text{FEM}}\right| , \tag{4}$$

where $\mathrm{h}^{\mathrm{k}}(\varepsilon^g_{i,j})^{\text{3D-XRD}}$ and $\mathrm{h}^{\mathrm{k}}(\varepsilon^g_{i,j})^{\text{FEM}}$ denote, respectively, the relative number of grains in the k^{th} histogram bar of 3D-XRD- and simulation-based equally binned distributions of grain-wise averaged strain tensor component $\varepsilon^g_{i,j}$, N_h is the number of bins.

The combinations of elastic constants have to provide average elastic properties in agreement with the measured quantities. In the present paper, the axial stress in the wire σ^{exp}_{zz} was measured by a load cell and the elastic axial deformation ε^{exp}_{zz} was calculated from the applied displacement (see Fig. 1a). Therefore, the average axial Young's modulus defined as $E^{exp} = \sigma^{exp}_{zz}/\varepsilon^{exp}_{zz}$ is known from the experimental data. Hence, the average Young's modulus ($\langle E^g_{zz}\rangle^{\text{3D-XRD}} \equiv \langle E^g_{33}\rangle^{\text{3D-XRD}}$), calculated over the total number of grains N_g, has to be equal to the experimentally identified Young's modulus E^{exp}. The average Young's modulus $\langle E^g_{zz}\rangle^{\text{3D-XRD}}$ could be calculated without considering the grain-wise averaged strains in individual grains by classical homogenization theories such as isostrain (Voigt), isostress (Reuss) or their average (Hill) [33] as well as by more advanced approaches, e.g., Kroner [34]. However, the 3D-XRD dataset enables to express the average Young's modulus in terms of directly measured grain-wise averaged strains

$\varepsilon_{i,j}^{g,\text{3D-XRD}}$ and the tested elasticity tensor $C_{i,j,k,l}^{g,test}$, formed from considered combination of elastic constants and expressed in the laboratory coordinate system for individual grains. This condition is formulated in the following equation:

$$\langle E_{zz}^{g}\rangle^{\text{3D-XRD}} \equiv \langle E_{33}^{g}\rangle^{\text{3D-XRD}} = \frac{\frac{1}{N_g}\sum_{g=1}^{N_g}\sum_{k=1}^{3}\sum_{l=1}^{3} C_{33kl}^{g,test}\varepsilon_{kl}^{g,\text{3D-XRD}}}{\langle \varepsilon_{33}^{g}\rangle^{\text{3D-XRD}}} = E^{exp}. \qquad (5)$$

If Condition (5) is not satisfied, the considered combination of elastic constants has to be excluded. The number of combinations of elastic constants is defined by finite sets of elastic constants C_{11}, C_{12}, C_{44} spanning around the initial constants C_{11}^{ini}, C_{12}^{ini}, C_{44}^{ini}. The set is then reduced by Condition (5), which in fact can be geometrically expressed in the space C_{11}, C_{12}, $\langle E_{33}^{g}\rangle^{\text{3D-XRD}}$ visualized in Fig. 5. Condition (5) delimits, for a constant C_{44}, the eligible combinations of C_{11}, C_{12} that belong to the intersection of the surface $\langle E_{33}^{g}\rangle^{\text{3D-XRD}}(C_{11}, C_{12})$ with the plane $\langle E_{33}^{g}\rangle^{\text{3D-XRD}} = E^{exp}$. This operation is performed for all C_{44} in the predefined set, which may result in multiple intersections and, hence, eligible combinations as shown schematically in Fig. 5.

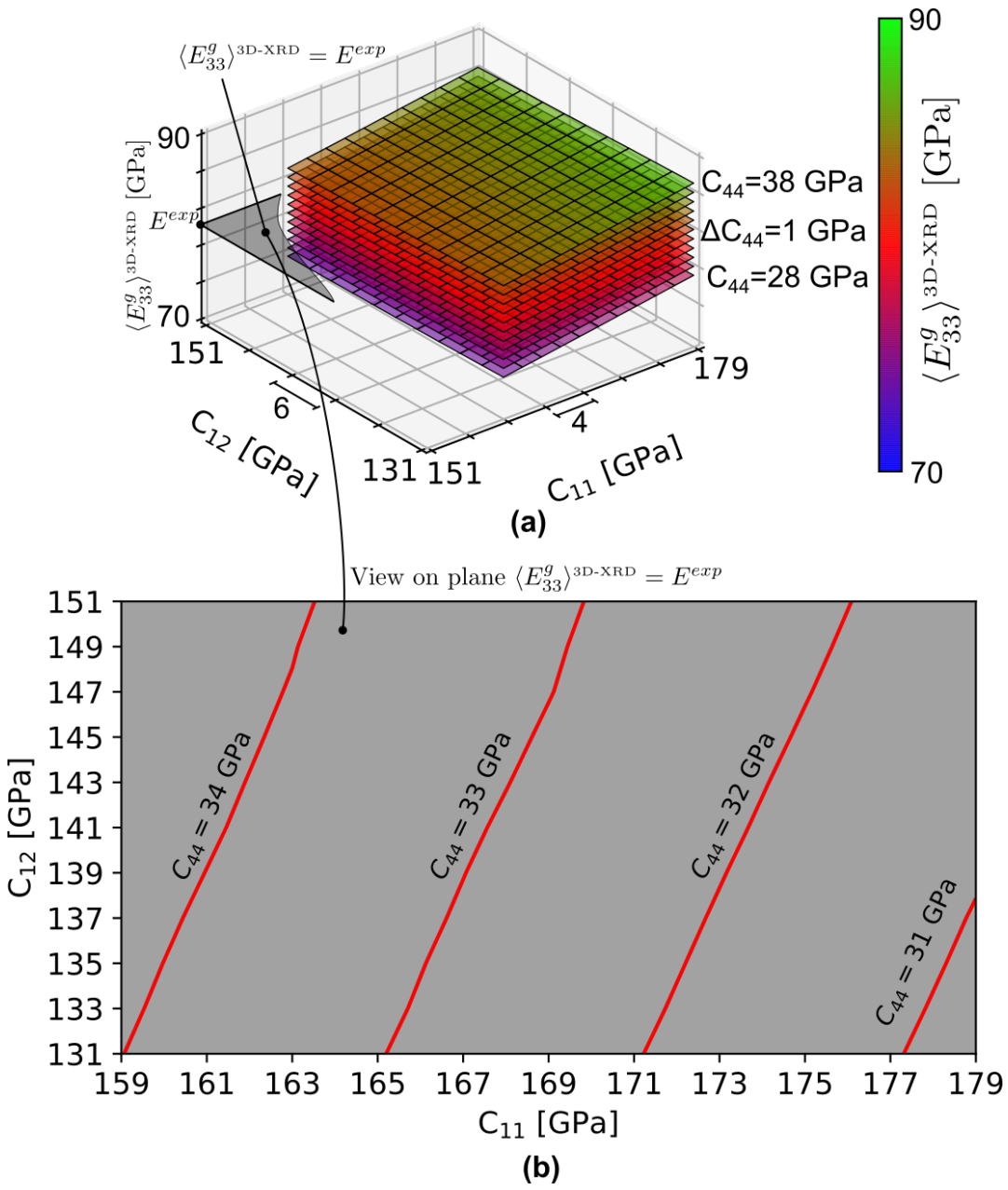

Figure 5. Illustration of how combinations of elastic constant are delimited for elastic anisotropy refinement. The eligible combinations for a given C_{44} constant belong to the intersection of the experimentally identified Young's modulus plane E^{exp} with the surface of the average Young's modulus $\langle E^g_{33}\rangle^{\text{3D-XRD}}$ calculated in the space of C_{11}, C_{12} using Eq. 5. Considering a set of C_{44} constants, multiple Young's modulus surfaces are constructed (a) resulting in multiple intersection lines (b).

4. Results

4.1. Reconstruction of microstructure morphology

The optimization algorithms (CE, Neper) considered in this paper converged to statistically similar microstructures as summarized in Fig. 6 and 7. Note that Laguerre

tessellations allow the removal of grains from the 3D-XRD dataset as it allows for generators with empty cells [3]. Consequently, the obtained number of grains may be smaller than the number of grains in the 3D-XRD dataset being reconstructed [7]. Indeed, in the case of the models CE and Neper the number of reconstructed grains was 7685 and 7949, respectively, compared to 8063 grains contained in the 3D-XRD dataset. From a statistical point of view, both models generate a higher number of small grains compared to the 3D-XRD dataset as indicated by the left tails of the red colored distributions, related to regularized microstructure FEM models, shown in Fig. 6b1,b2, that do not overlap with the green distribution related to the 3D-XRD dataset. Mean and standard deviation of grain sizes differ from the 3D-XRD dataset by less than 10 % of the average grain size (5.1 μm). Grain by grain comparisons between the models and the 3D-XRD dataset show nearly symmetrical distributions of differences in grain sizes with standard deviations in the range 1.20-1.30 μm (Fig. 6c1,c2). Grains in the CE and Neper models are in average misplaced by 1.05 and 0.92 μm, respectively, from the grain center-of-mass positions provided by the 3D-XRD dataset, while the standard deviation of the misplacement is equal to 1.94 and 1.81 μm, respectively (Fig. 6d1,d2). Note that the mean values and the standard deviations of the distributions shown in Fig. 6 were evaluated by fitting the data using normal density functions (for the grain sizes and the differences in grain sizes) or using log-normal density functions (for the errors in grain center-of-mass positions).

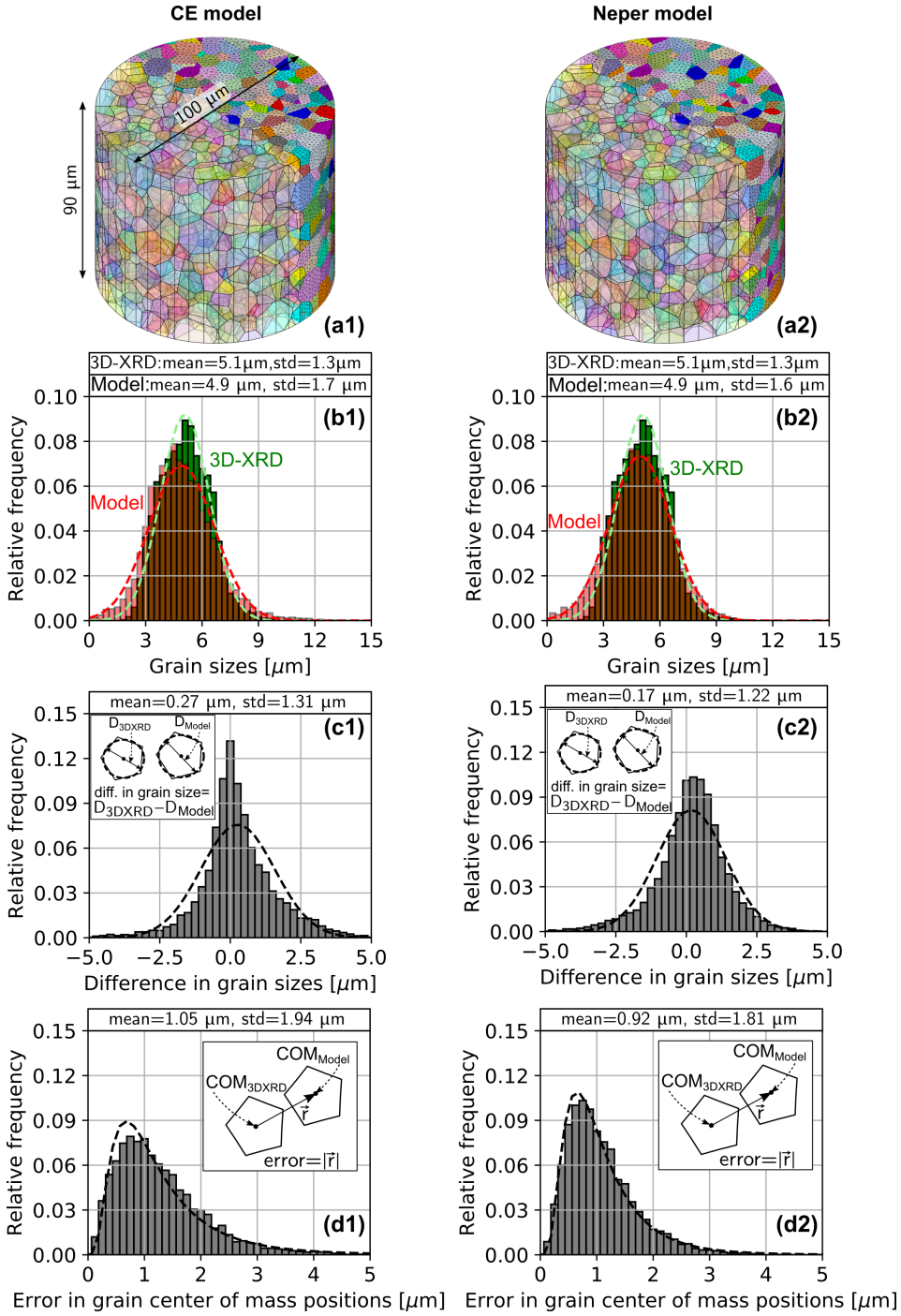

Figure 6. Histograms on the left (CE model) and right (Neper model) show the agreement of regularized microstructure models based on CE (a1) and Neper (a2) with the 3D-XRD dataset in terms of grain size distributions (b1), (b2), where the red distributions denoted by Model fitted by normal density functions (red dashed curves) are related to models while the green ones denoted by 3D-XRD are related to the 3D-XRD dataset. Furthermore, the misfit between the results obtained by the microstructure models and the 3D-XRD dataset is evaluated in terms of distributions of differences of grain size fitted by normal density functions (c1), (c2) and center-of-mass positions fitted by log-normal density functions (d1), (d2).

In terms of the grain shape and number of neighbors both algorithms delivered exactly the same statistics as seen in Fig. 7. Both models lead to a mean sphericity of the grains of 0.77 with a standard deviation of 0.09 (Fig. 7a1,a2). On average the grains have 11 neighbors in both models as shown in Fig. 7b1,b2.

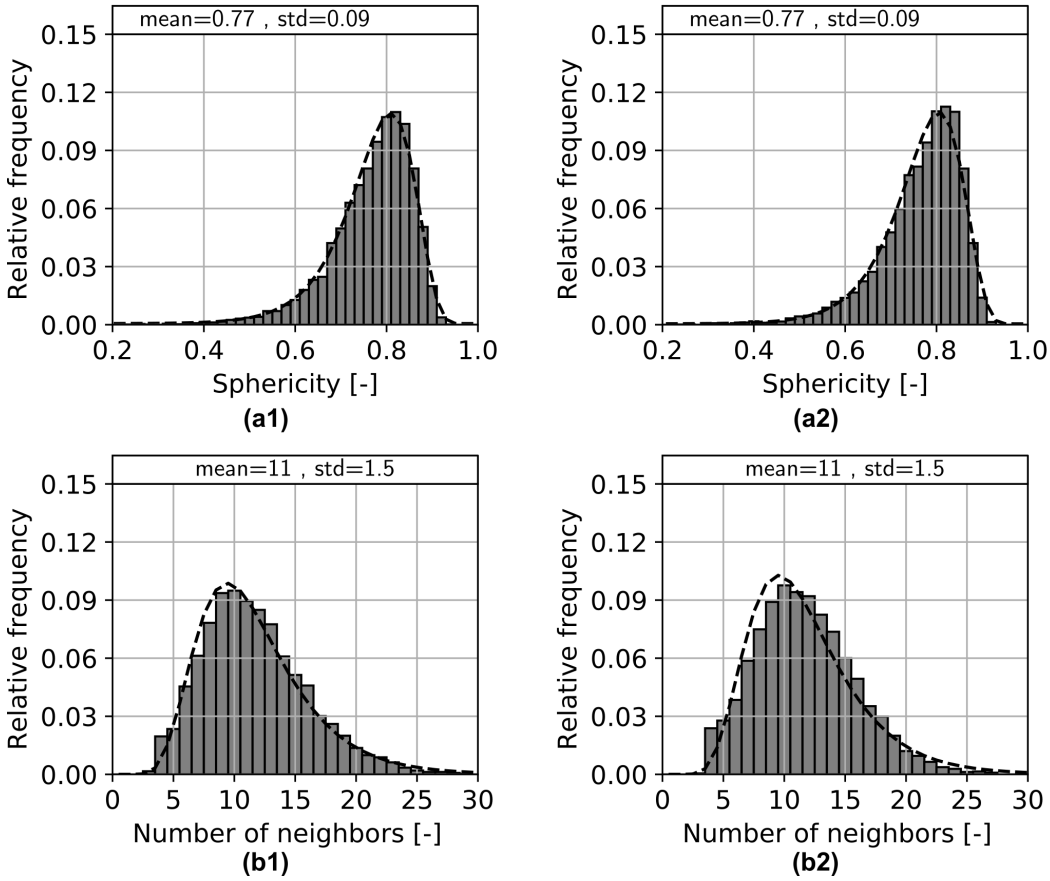

Figure 7. Histograms fitted by log-normal density functions (dashed curves) representing the unweighted distributions of grain sphericities (a1), (a2) and numbers of grain neighbors (b1), (b2) for the microstructure models of NiTi wire considered in this paper: CE (left) and Neper (right).

4.2. Finite element microstructure models

Table 1 summarizes key figures of finite element microstructure models in terms of total and per grain number of elements and nodes. The CE and Neper models were discretized by ∼1.5 and ∼1.0 million elements, respectively, corresponding to 202 and 136 elements per grain on average. In terms of number of nodes, the CE model contained ∼260,000 nodes in the linear element version and ∼2.1 million nodes in the quadratic element version. The Neper model was prepared in the linear version only containing ∼187,000 nodes.

Table 1. Number of elements and nodes used in the finite element discretization of the two microstructure models.

		Number of elements		Number of nodes linear/**quadratic** elements	
	Number of grains	total number	mean per grain	total number	mean per grain
CE model	7685	1,555,401	202	266,423/**2,105,803**	78/**410**
Neper model	7949	1,081,699	136	187,463/**1,474,082**	57/**276**

4.3. Initial elastic anisotropy: 3D-XRD vs. microstructure models

The numerical microstructure models were first considered with the initial elastic constants C_{11}^{ini}=169 GPa, C_{12}^{ini}=141 GPa, and C_{44}^{ini}=33 GPa in agreement with experimentally identified values in stress-free conditions [21]. Note that these constants correspond to rather low anisotropy of elastic properties (anisotropy factor of 2.36). Three simulations were performed in order to test the sensitivity of the simulation results with respect to the microstructure models (CE model vs. Neper model) and the two types of discretization (linear vs. quadratic elements). The specifications of all types of structural static simulations performed with the initial elastic constants are listed in Table 2,including also computational times. All simulations were run on a single CPU of a computational cluster with 50 GB and 300 GB of allocated RAM for models discretized with linear and quadratic elements, respectively.

Table 2. Specifications of the simulations performed to assess the sensitivity of numerical microstructure models to the degree of finite element discretization and type of Laguerre tessellation optimization.

Simulation name	Reconstruction algorithm		Type of finite elements		Computational time [h]
	CE model	Neper model	Linear	Quadratic	
FEM CE LIN	•		•		0.30
FEM CE QUAD	•			•	15
FEM NE LIN		•	•		0.17
FEM NE QUAD		•		•	8

Table 3 compares the 3D-XRD measurements with the results of the three simulations in terms of mean values (the upper part of Table 3) and standard deviations (the lower part of the Table 3) of grain-wise averaged distributions of strain and stress tensor components. Clearly, all three simulations provided nearly identical statistical results, which agreed well with the mean values of the 3D-XRD dataset (see the upper part of Table 3). However, the standard deviations from 3D-XRD and simulations

do not match (see the lower part of Table 3). This fact is further evidenced by Fig. 8 directly comparing the distributions of grain-wise averaged strains and stresses as provided by 3D-XRD and the CE model. Furthermore, grain-by-grain comparisons between 3D-XRD and the simulation are shown in Fig. 9 in terms of 2D distributions for all components of the grain-wise averaged stresses. For an ideal case of a perfect match between the 3D-XRD dataset and the model, the 2D distributions are expected to reduce into lines coinciding with the red identity line. However, it is not the case nor are the major axes of the distributions aligned with the identity line. A perfect grain-to-grain match of the grain-wise averaged stresses was not reached as like the grain sizes and the grain positions did not perfectly match the 3D-XRD dataset as shown in Fig. 6c,d. Note that the widths of the 2D distributions along their minor axes seem to correlate with the widths and standard deviations of the 1D histograms of the grain-wise averaged stresses shown in Fig. 8g-k, .i.e, the 2D distributions and the 1D histograms of the normal stress components are broader compared to those of the shear stress components.

Table 3. Mean values (upper part of the rows indicated by 'Mean') and standard deviations (lower part of the rows indicated by 'STD') of the distributions of grain-wise averaged components of strain and stress tensors in individual grains of NiTi wire under axial tension as provided by the 3D-XRD method and simulated by numerical microstructure models according to Table 2.

		Strain distributions [%]						Stress distributions [MPa]					
		ε_{rr}	$\varepsilon_{\theta\theta}$	ε_{zz}	$\varepsilon_{\theta r}$	ε_{zr}	$\varepsilon_{z\theta}$	σ_{rr}	$\sigma_{\theta\theta}$	σ_{zz}	$\sigma_{\theta r}$	σ_{zr}	$\sigma_{z\theta}$
3D-XRD	Mean	-0.21	-0.21	0.52	0.00	0.06	0.00	-1	3	420	0	6	0
FEM CE LIN	Mean	-0.21	-0.21	0.51	0.00	0.05	0.00	2	1	423	0	1	0
FEM CE QUAD	Mean	-0.21	-0.21	0.52	0.000	0.05	0.00	-2	1	423	0	1	0
FEM NE LIN	Mean	-0.21	-0.21	0.51	0.00	0.02	0.00	-1	-1	425	0	0	0
FEM NE QUAD	Mean	-0.21	-0.21	0.52	0.00	0.02	0.01	-1	-1	424	0	0	0
3D-XRD	STD	0.06	0.06	0.05	0.06	0.08	0.08	69	70	62	30	31	30
FEM CE LIN	STD	0.03	0.03	0.03	0.03	0.03	0.03	31	32	35	20	22	23
FEM CE QUAD	STD	0.04	0.04	0.04	0.03	0.04	0.04	30	31	34	18	20	20
FEM NE LIN	STD	0.03	0.03	0.03	0.02	0.04	0.04	31	32	35	20	23	23
FEM NE QUAD	STD	0.04	0.04	0.04	0.03	0.05	0.05	31	32	36	18	20	20

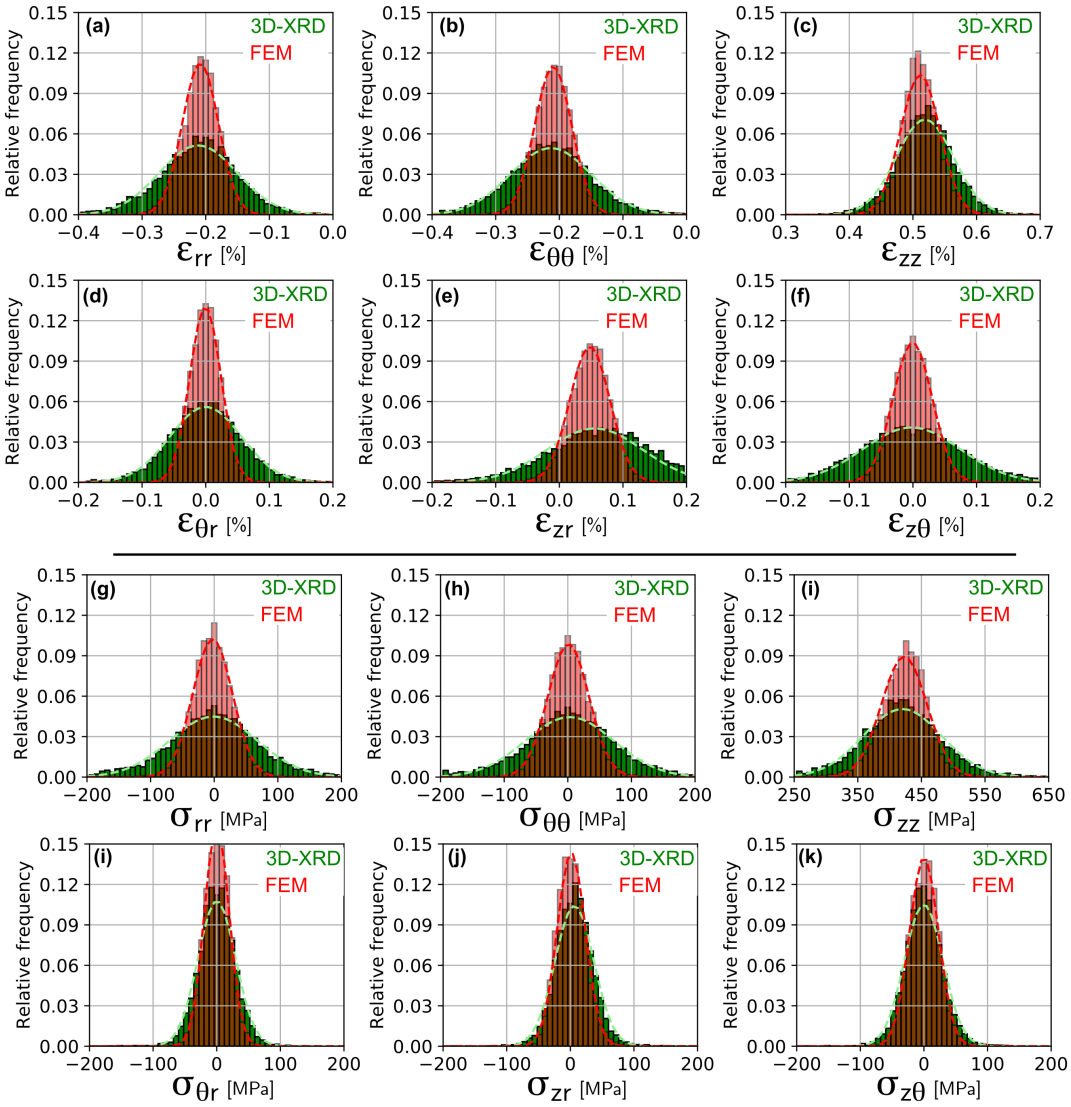

Figure 8. Histograms fitted by normal density functions (dashed curves) representing distributions of grain-wise averaged strain (a-f) and stress (g-l) tensor components as provided by 3D-XRD (green) and FEM simulation (red) using linear elements, microstructures based on the CE model, and initial elastic constants.

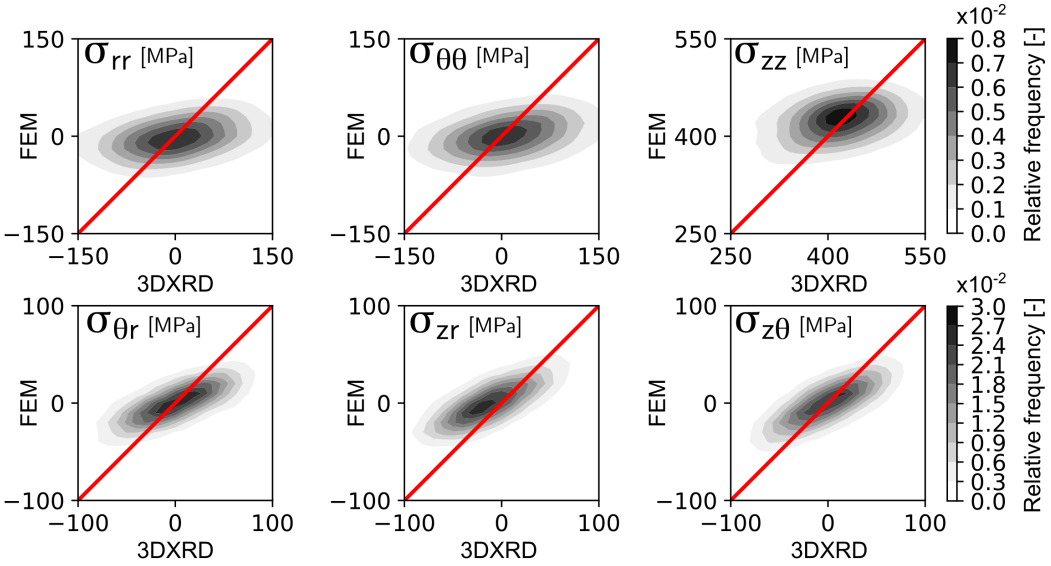

Figure 9. Gaussian kernel density estimates for all components of grain-wise averaged stresses between stresses measured by 3D-XRD and simulated by FEM using linear elements, microstructures based on the CE model, and the initial elastic constants.

4.4. Refinement of elastic anisotropy

The elastic anisotropy was refined using the microstructure based on the CE model and linear elements. The refinement was split into two steps. First, a rough refinement in a neighborhood of the initial elastic constants C_{11}^{ini}, C_{12}^{ini}, C_{44}^{ini} was performed in order to identify the range of anisotropy factors where the minimum discrepancy in standard deviations of grain-wise averaged strains would be localized. Then a second refinement was performed within this range considering a set of finely incremented elastic constants. The rough refinement was based on C_{11}, C_{12} sets spanned $\pm$ 10 GPa from C_{11}^{ini}, C_{12}^{ini} using increments of 2 GPa, i.e., $C_{11} \in \{159, 161, 163, \ldots, 179\}$, $C_{12} \in \{131, 133, 135, \ldots, 151\}$ while the C_{44} set spanned $\pm$ 5 GPa from C_{44}^{ini} using increments of 1 GPa, i.e., $C_{44} \in \{28, 29, 30, \ldots, 38\}$. As detailed in Section 3.3, the number of possible combinations of elastic constants around the initial ones is limited by the requirement on the value of average axial Young's modulus, cf. Eq. 5. However, for the rough refinement this condition was relaxed by allowing $\pm$ 10 GPa discrepancy from the value of average axial Young's modulus. Furthermore, a requirement on the anisotropy factor equal to or larger than 3 was considered. This requirement is based on the fact that standard deviations of grain-wise averaged stresses increase with increasing anisotropy factor and that preliminary simulations using anisotropy factors up to 3 showed standard deviations being still small compared to 3D-XRD measurements. Using this conditioning a set of 52 combinations of elastic constants was generated spanning the anisotropy factor from 3 to 8 as visualized in Fig. 10.

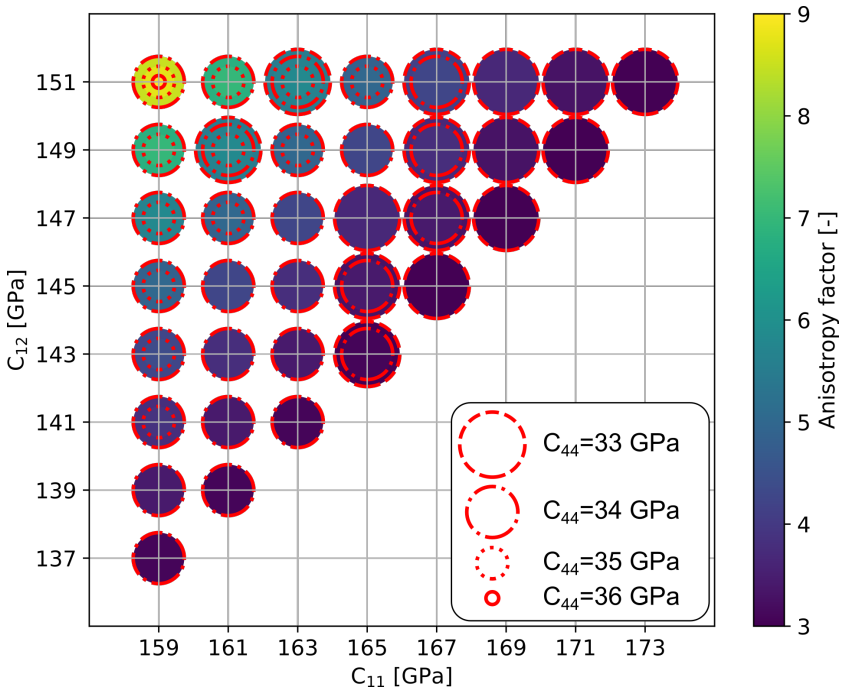

Figure 10. Set of combinations of elastic constants and related anisotropy factors as considered for the rough refinement of elastic anisotropy.

The absolute difference in standard deviations of grain-wise averaged strains according to Eq. 3 was evaluated between 3D-XRD and the simulations realized on the complete set of combinations of elastic constants. The results of these evaluations are visualized in Fig. 11 showing minima in the upper-left corner where anisotropies ranging from 6 to 7 are located (compare Fig. 10 and 11). The mismatch between 3D-XRD and the simulations as it evolves with the anisotropy factor is visualized in Fig. 12 in terms of absolute difference in standard deviations of grain-wise averaged strains evaluated according to Eq. 3 and L_1-based metrics evaluated according to Eq. 4. Both metrics show a minimum located in the range of the anisotropy factors 5 to 7. However, the metrics did not reach the zero values at these minima, indicating that the perfect match of the simulations with 3D-XRD was not reached.

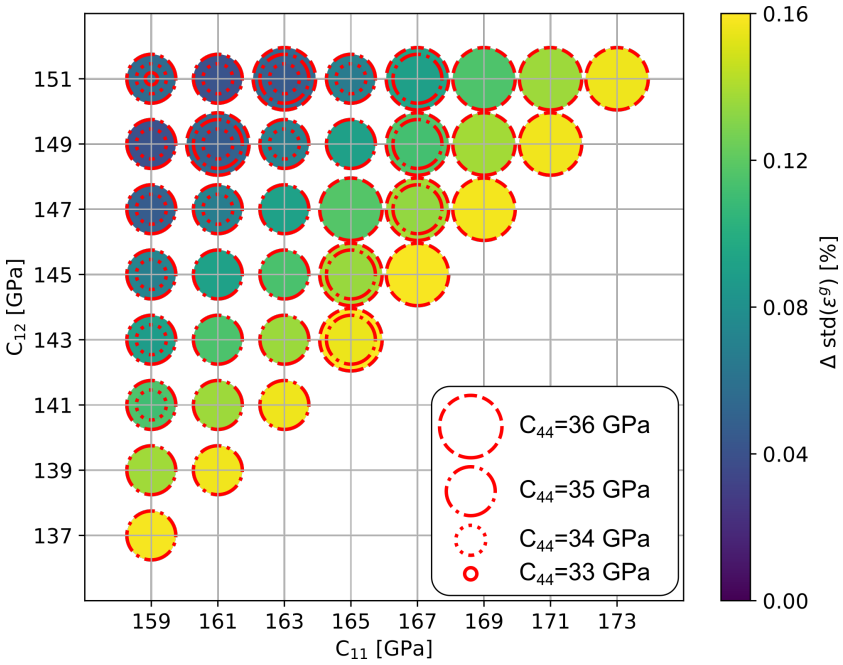

Figure 11. Absolute differences in standard deviations of grain-wise averaged strains (Eq. 3) evaluated between 3D-XRD and the simulations for all combinations of elastic constants considered in the rough refinement of elastic anisotropy.

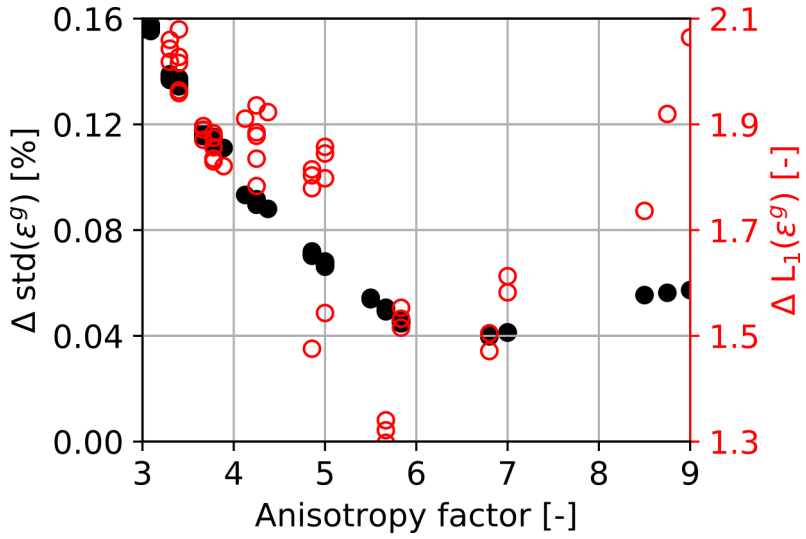

Figure 12. Evolution of the statistical match between 3D-XRD and the simulations with increasing elastic anisotropy. The match was evaluated in terms of standard deviation as the sum of absolute differences in standard deviations of grain-wise averaged strain (Eq. 3) components and using L_1 norm according to (Eq. 4).

The anisotropy factor was further refined in the range 6-8 by considering sets of elastic constants $C_{11} \in \{149, 150, 151, \ldots, 189\}$, $C_{12} \in \{121, 122, 123, \ldots, 161\}$, and $C_{44} \in \{32, 32.2, 32.4, \ldots, 36\}$. The eligible combinations of elastic constants were found by imposing the condition of the average Young's modulus (Eq. 5) and by using the method described in Section 3.3. As a result a set of 99 elastic constants distributed in

the space C_{11},C_{12},C_{44} as shown in Fig. 13 was considered. Within the space C_{11}, C_{12}, C_{44} minima of the absolute difference in standard deviations of grain-wise averaged strains according to Eq. 3 were again identified as shown in Fig. 14 and a minimum was identified with respect to the anisotropy factor as shown by black filled dots in Fig. 15. This minimum coincides reasonably well with the minimum in the evolution of L_1-based metrics evaluated according to Eq. 4 with respect to the anisotropy factor and shown by red empty dots in Fig. 15.

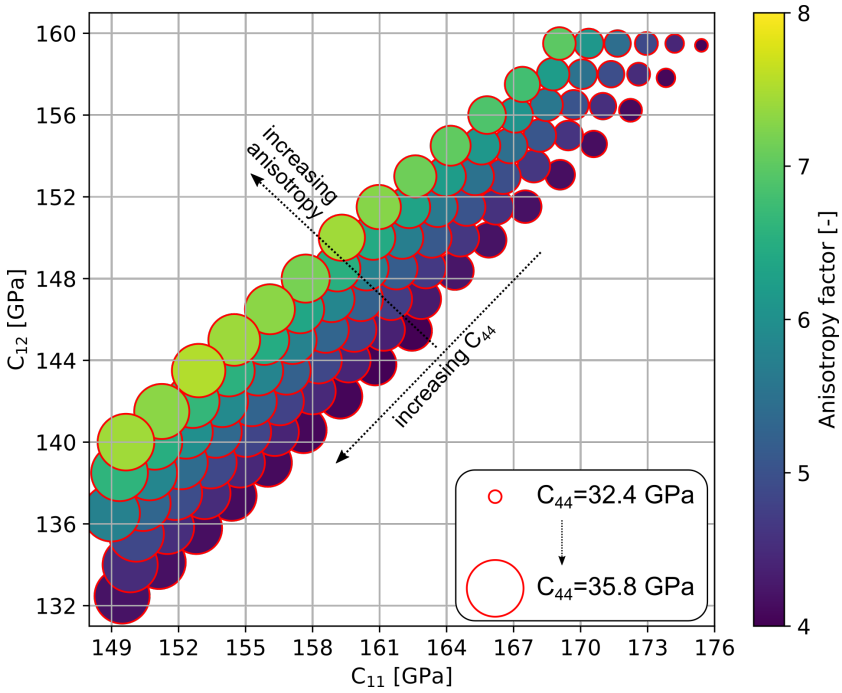

Figure 13. Set of combinations of elastic constants and corresponding anisotropy factors as considered for the fine refinement of elastic anisotropy.

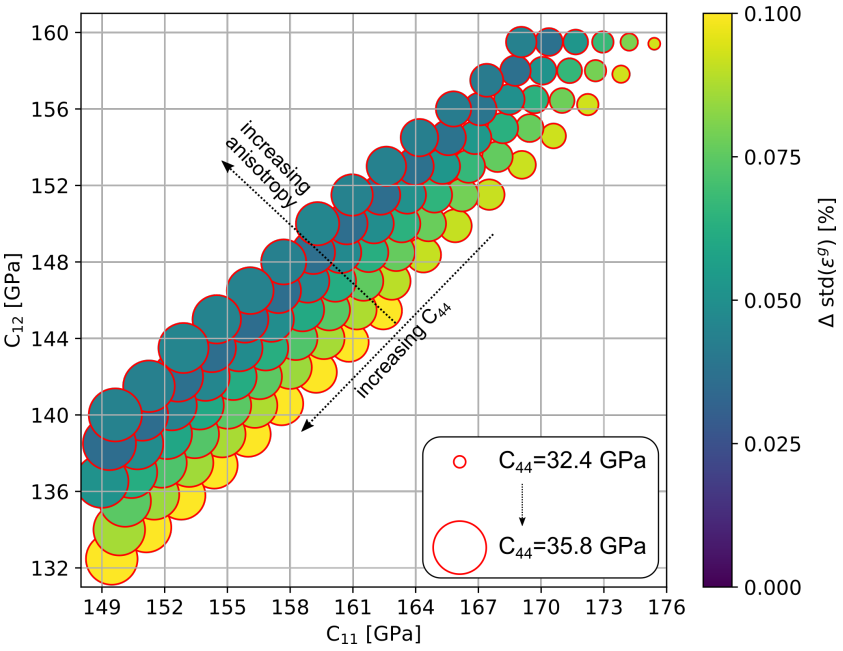

Figure 14. Absolute differences in standard deviations of grain-wise averaged strains (Eq. 3) evaluated between 3D-XRD and the simulations for all combinations of elastic constants considered in the fine refinement of elastic anisotropy.

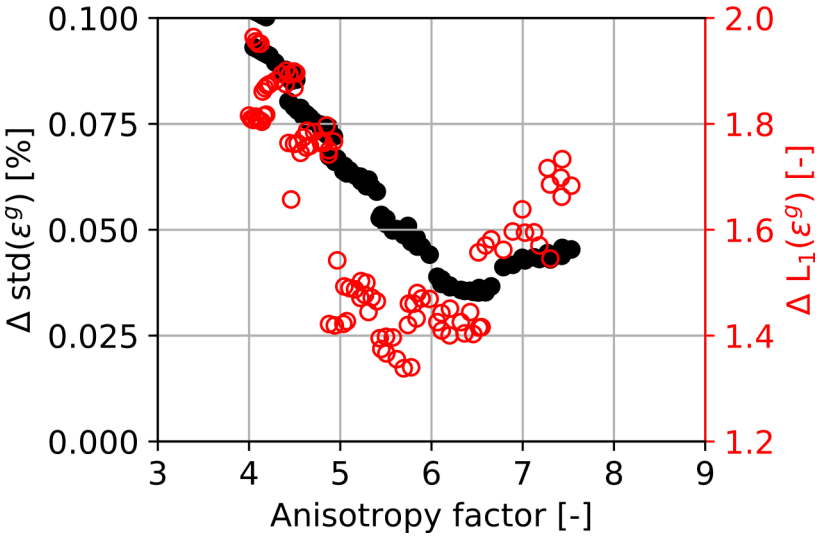

Figure 15. Evolution of the statistical match between 3D-XRD and the simulations with increasing elastic anisotropy. The match was evaluated for all combinations of elastic constants considered in the fine refinement of elastic anisotropy in terms of the sum of absolute differences in standard deviations of grain-wise averaged strain components (Eq. 3) and using L_1 norm according to (Eq. 4)..

4.5. Refined elastic anisotropy: 3D-XRD vs. microstructure CE model

Based on the elastic anisotropy refinement, the combination of elastic constants C_{11}=159 GPa, C_{12}=147 GPa, C_{44}=35 GPa (anisotropy factor of 6.2) was selected in this section to illustrate the statistical match of the microstructure model with the 3D-XRD dataset. Table 4 compares the results based on the 3D-XRD dataset with simulation results for the microstructure based on the CE model with initial elastic constants (CE model INI) and those selected from the refinement of elastic anisotropy (CE model REF). Table 4 clearly shows a close match of the 3D-XRD dataset with the refined model in terms of standard deviations (the lower part of Table 4) of grain-wise averaged distributions of strain and stress tensor components. This statistical match of the 3D-XRD dataset with the refined model is further illustrated by Fig. 16 directly comparing distributions of grain-wise averaged strains and stresses as provided by 3D-XRD and the CE model. Related 2D distributions of the grain-wise averaged stress components measured by 3D-XRD and simulated using the refined elastic constants are shown in Fig. 17, where the scales are identical to the scales used in Fig. 9 related to the initial elastic constants. Unlike in the case of the initial elastic constants, the major axes of the distributions are aligned with the red identity line. On the other hand, the distributions broadened along the vertical simulation axes. The broadening is suggested to be due to the increased elastic anisotropy analogically to its broadening effect on the the widths of the 1D histograms of the grain-wise averaged stresses simulated with the initial and refined elastic constants. The broadening of the 2D distributions reflects an increased stress scattering among outliers, i.e., among the grains lying above and below the red identity line that do not match the stresses of their experimental counterparts. Note that the broadening is more pronounced in the case of the normal stress components compared to the shear stress components similarly to the 1D histograms of the grain-wise averaged stresses (Fig. 16) that are broader in the case of the normal stress components.

Table 4. Mean values (upper part of the rows indicated by 'Mean') and standard deviations (lower part of the rows indicated by 'STD') of distributions of grain-wise averaged components of strain and stress tensors in individual grains of the NiTi wire under axial tension as provided by 3D-XRD method and simulated by the numerical microstructure based on the CE model using the initial (CE model INI) and the refined elastic anisotropy (CE model REF).

		Strain distributions [%]						Stress distributions [MPa]					
		ε_{rr}	$\varepsilon_{\theta\theta}$	ε_{zz}	$\varepsilon_{\theta r}$	ε_{zr}	$\varepsilon_{z\theta}$	σ_{rr}	$\sigma_{\theta\theta}$	σ_{zz}	$\sigma_{\theta r}$	σ_{zr}	$\sigma_{z\theta}$
3D-XRD	Mean	-0.21	-0.21	0.52	0.00	0.06	0.00	0	7	419	0	-10	0
CE model INI	Mean	-0.21	-0.21	0.51	0.00	0.05	0.00	2	1	423	0	1	0
CE model REF	Mean	-0.22	-0.22	0.54	0.00	0.10	0.00	-5	1	427	0	3	0
3D-XRD	STD	0.06	0.06	0.05	0.06	0.08	0.08	74	75	67	41	40	40
CE model INI	STD	0.03	0.03	0.03	0.03	0.03	0.03	31	32	35	20	22	23
CE model REF	STD	0.06	0.06	0.05	0.06	0.06	0.06	59	61	59	38	39	40

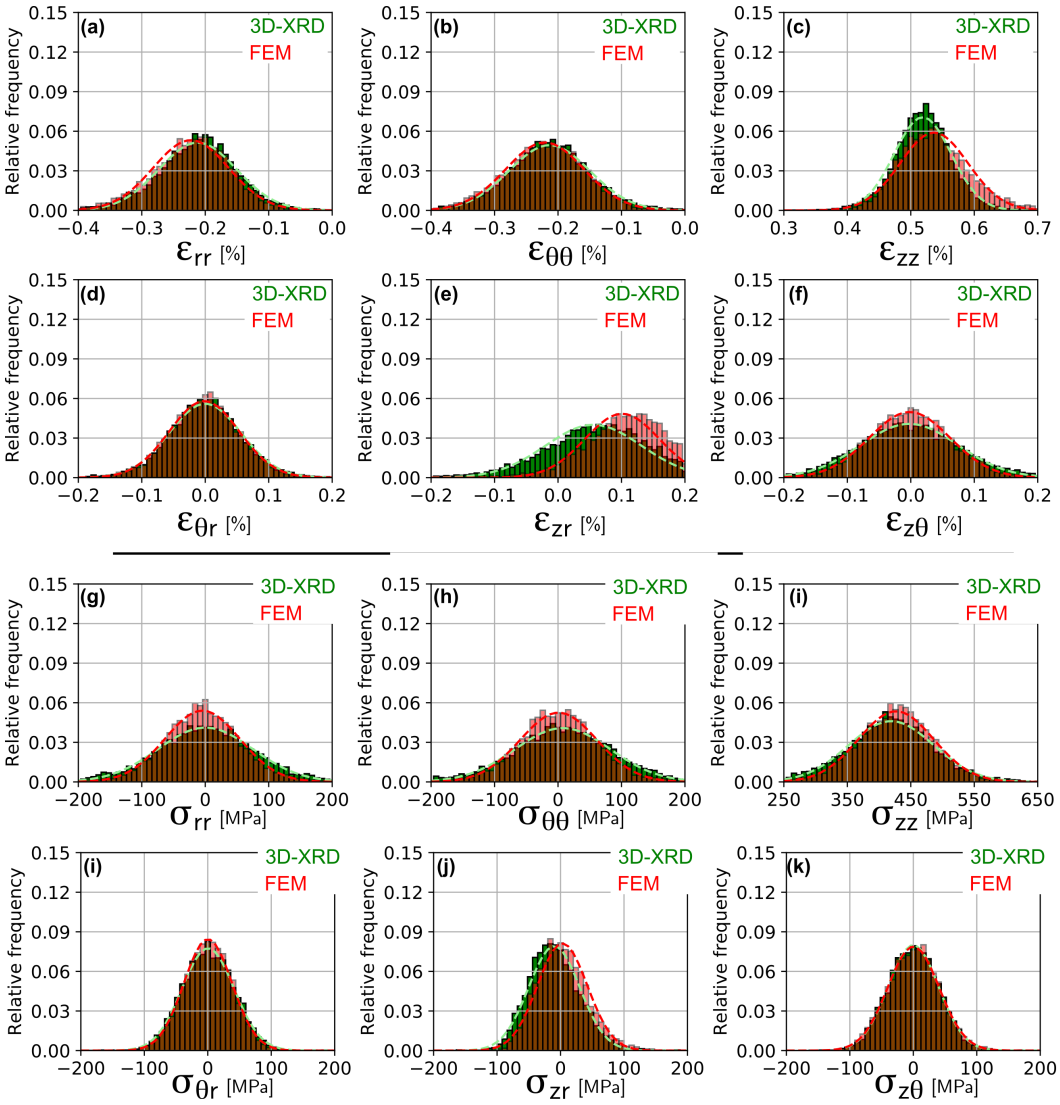

Figure 16. Histograms fitted by normal density functions (dashed curves) representing distributions of grain-wise averaged strain (a-f) and stress (g-l) tensor components as provided by 3D-XRD (green) and simulations (red) using the CE model of microstructure and refined elastic anisotropy.

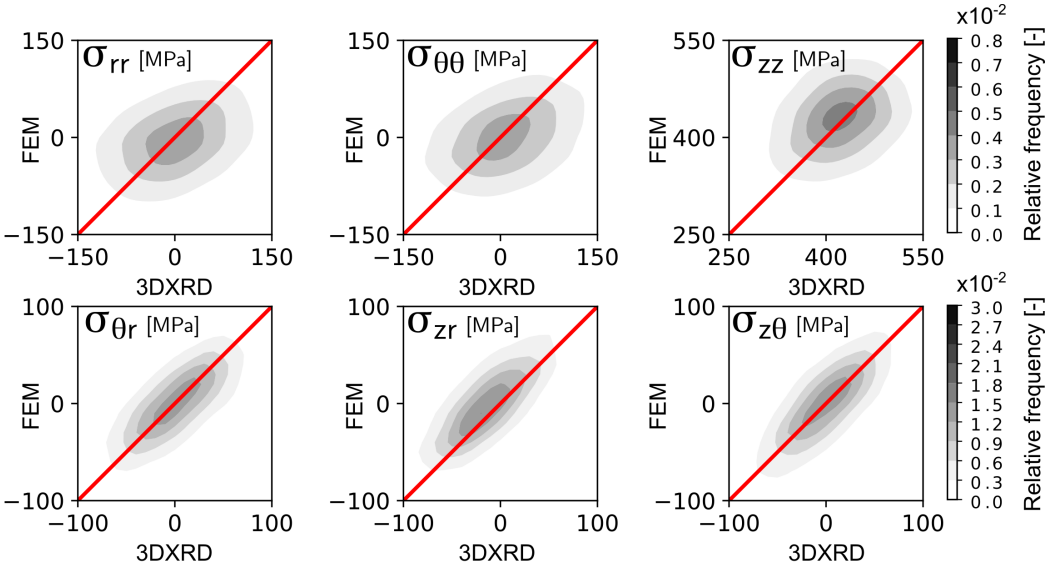

Figure 17. Gaussian kernel density estimates for all components of grain-wise averaged stresses between stresses measured by 3D-XRD and simulated by FEM using linear elements, microstructures based on the CE model, and the refined elastic anisotropy.

5. Discussion

Elasticity is the fundamental deformation mechanism that results in elastic interactions of grains within the polycrystalline aggregate. These interactions determine the stress fields triggering other stress-induced deformation mechanisms such as plasticity, martensitic transformation or deformation twinning. These are often initiated at local specific stress states, which are induced by combined effects of elastic anisotropy and grain interactions. The presented comparisons between the 3D-XRD dataset and simulation results suggest that Laguerre tessellations can generate microstructure models that realistically predict the elastic interactions of grains within polycrystalline aggregates. Moreover, it follows from our results that Laguerre tessellations provide realistic microstructure models irrespectively of the applied optimization procedure. The statistical disagreement between the 3D-XRD dataset and the simulations summarized in Table 4 and Fig. 16 may be ascribed to the disagreement in morphological features of microstructures summarized in Fig. 6 and to limitations of both experimental techniques (unidentified grains, limited accuracy of strain determination) and Laguerre tessellations (empty cells, planar grain boundaries, convex grains).

In order to realistically simulate the process of, e.g., stress-induced MT, the values of the elastic constants prior to the phase transformation have to be known as they determine the stress field and critical local stress states that may trigger the local phase transformation. The magnitude of stress inhomogeneities is proportional to the elastic anistropy defined by elastic constants. In this paper, we show that the change in elastic anisotropy can be determined from a simple optimization scheme. For this, a combination of elastic constants is sought which globally minimizes the mismatch of stress and strain between the experimental measurements and the simulations based on a morphologically realistic model.

Locally, however, the grain-by-grain comparisons 3D-XRD vs. model in terms of the grain-wise averaged stresses revealed 2D distributions (Fig. 17) showing that a perfect match in the elastic deformation behavior was not reached. This may be sought as a

consequence of the mismatch in the morphological parameters between the 3D-XRD and the model evaluated in Fig. 6. In fact, Fig. 6b shows that the global statistics of the grain sizes is nearly matched by the model. However, on the grain-by-grain basis the grain sizes scatter from the experimental values by 20% of the mean grain size on average. Similarly, the grain positions are on average misplaced by 20% from the experimentally identified positions. This mismatch may be ascribed to the incompleteness of the microstructure data provided by the 3D-XRD method. Nevertheless, the model was reconstructed from a statistically significant dataset, informing about thousands of grains. Therefore, the model reconstructed from such a 3D-XRD dataset is expected to match the global statistics about the microstructure and the deformation behavior. The model should be able to predict the statistics of the grain interactions due to deformation mechanisms that are experimentally difficult to be studied by grain-resolved methods, e.g., the stress-induced MT, provided that the deformation mechanism is properly mathematically described in the model. To this end, the model should also predict statistics of the elastic behavior that are not accessible by 3D-XRD method, e.g., the distribution of critical local stress maxima in the grains. This distribution can significantly differ from the distribution of grain-wise averaged stresses in terms of both mean values and standard deviations as illustrated in Fig. 18, where we compare the distributions of the grain-wise averaged axial stresses (Fig. 18a) and the grain-wise maxima of axial stresses (Fig. 18b) resulting from finite element simulations based on the CE model with the lower initial elastic anisotropy of 2.4 (dark red distributions in Fig. 18) and the higher refined elastic anisotropy of 6.2 (light red distributions in Fig. 18). Clearly, the increased anisotropy induced not only a considerably higher scatter in the local stress maxima but also an increase in the average value (Fig. 18b) although the mean value of the grain-wise averaged stresses was not affected by the increased elastic anisotropy (Fig. 18a).

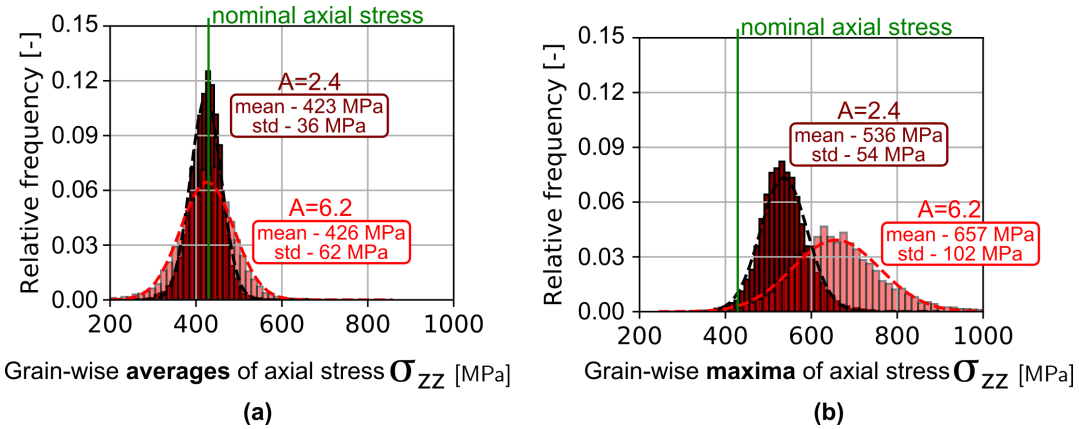

Figure 18. Comparison of results for simulations using the microstructure based on the CE model with initial elastic anisotropy (dark red) and refined elastic anisotropy (light red) in terms of histograms fitted by normal density functions (dashed curves) representing distributions of grain-wise averaged axial stresses (a) and grain-wise maxima of axial stresses (b).

6. Conclusions

In the present paper the grain microstructure and strain partitioning in a polycrystalline NiTi wire subjected to tensile loading was reconstructed from an experimental 3D-XRD

dataset. The microstructure morphology was reconstructed by Laguerre tessellations optimized on grain center-of-mass positions and sizes of individual grains provided by the 3D-XRD dataset. Two optimization algorithms were tested, both of them led to similar microstructure morphologies. The fundamental elastic deformation behavior of the model was prescribed in terms of grain orientations provided by the 3D-XRD dataset and the elastic properties of the cubic austenite phase. The initial anisotropy of elastic properties according to published elastic constants was refined through an optimization process driven by the mismatch in standard deviations (scatters) of grain-wise averaged strain component distributions measured by 3D-XRD and obtained from finite element simulations, respectively. The results of the optimization suggest that the elastic anisotropy of the austenite under stress is higher compared to the anisotropy calculated from the values of elastic constants experimentally evaluated by ultrasonic methods. A close match between the 3D-XRD dataset and the model with refined elastic anisotropy was found in terms of the distributions of grain-wise averaged strain and stress components. A realistic microstructure model of a NiTi wire matching the microstructure features as well as the elastic deformation behavior of the real microstructure was thus obtained. The model will be further used in micromechanical simulations of stress-induced MT in superelastic NiTi wires.

Acknowledgment

The authors acknowledge the financial support provided by Czech Science Foundation, project 17-00393J. L. Heller and P. Šittner acknowledge the financial support by Operational Programe Research, Development and Education financed by European Structural and Investment Funds and the Czech Ministry of Education, Youth and Sports, under the project "Solid 21", project No. SOLID21 - CZ.02.1.01/0.0/0.0/16_019/0000760, and under the project " European Spallation Source - participation of the Czech Republic - OP ", "Reg. No. CZ.02.1.01/0.0/0.0/16_013/0001794". Access to computing and storage facilities owned by parties and projects contributing to the National Grid Infrastructure MetaCentrum provided under the programe "Projects of Large Research, Development, and Innovations Infrastructures" (CESNET LM2015042), is greatly appreciated. Furthermore, this research was partially funded by the German Science Foundation (DFG, project number SCHM 997/23-1).

References

[1] Poulsen H F 2004 *Three-Dimensional X-Ray Diffraction Microscopy: mapping polycrystals and their dynamics* (Springer)
[2] Okabe A, Boots B, Sugihara K and Chiu S N 2000 *Spatial tessellations : concepts and applications of Voronoi diagrams* (Wiley)
[3] Lautensack C and Zuyev S 2008 *Advances in Applied Probability* **40** 630–650
[4] Hirsekorn S 1990 *Textures and Microstructures* **12** 1–14
[5] Zaefferer S and Wright S I 2009 Three-Dimensional Orientation Microscopy by Serial Sectioning

and EBSD-Based Orientation Mapping in a FIB-SEM *Electron Backscatter Diffraction in Materials Science* (Boston, MA: Springer US) pp 109–122
[6] Lyckegaard A, Lauridsen E M, Ludwig W, Fonda R W and Poulsen H F 2011 *Advanced Engineering Materials* **13** 165–170
[7] Petrich L, Staněk J, Wang M, Westhoff D, Heller L, Šittner P, Krill C E, Beneš V and Schmidt V 2019 *Microscopy and Microanalysis* **25** 743–752
[8] Quey R and Renversade L 2018 *Computer Methods in Applied Mechanics and Engineering* **330** 308–333
[9] Quey R, Dawson P and Barbe F 2011 *Computer Methods in Applied Mechanics and Engineering* **200** 1729–1745
[10] Roters F, Eisenlohr P, Hantcherli L, Tjahjanto D, Bieler T and Raabe D 2010 *Acta Materialia* **58** 1152–1211
[11] Gonzalez D, Simonovski I, Withers P and Quinta da Fonseca J 2014 *International Journal of Plasticity* **61** 49–63
[12] Abdolvand H, Majkut M, Oddershede J, Schmidt S, Lienert U, Diak B J, Withers P J and Daymond M R 2015 *International Journal of Plasticity* **70** 77–97
[13] Abdolvand H, Wright J and Wilkinson A J 2018 *Nature Communications* **9** 171
[14] Paranjape H M, Paul P P, Sharma H, Kenesei P, Park J S, Duerig T, Brinson L C and Stebner A P 2017 *Journal of the Mechanics and Physics of Solids* **102** 46–66
[15] Otsuka K and Wayman C M 1998 *Shape memory materials* (Cambridge University Press)
[16] Van Humbeeck J 2001 *Advanced Engineering Materials* **3** 837
[17] Chen Y, Molnárová O, Tyc O, Kadeřávek L, Heller L and Šittner P 2019 *Acta Materialia* **180** 243–259
[18] Chen Y, Tyc O, Kadeřávek L, Molnárová O, Heller L and Šittner P 2019 *Materials & Design* **174** 107797
[19] Robertson S W, Pelton A R and Ritchie R O 2012 *International Materials Reviews* **57** 1–36
[20] Alarcon E, Heller L, Chirani S A, Šittner P, Kopeček J, Saint-Sulpice L and Calloch S 2017 *International Journal of Fatigue* **95** 76–89
[21] Sedmák P, Pilch J, Heller L, Kopeček J, Wright J, Sedlák P, Frost M and Šittner P 2016 *Science (New York, N.Y.)* **353** 559–62
[22] Šittner P, Sedlák P, Seiner H, Sedmák P, Pilch J, Delville R, Heller L and Kadeřávek L 2018 *Progress in Materials Science* **98** 249–298
[23] Heller L, Šittner P, Sedlák P, Seiner H, Tyc O, Kadeřávek L, Sedmák P and Vronka M 2019 *International Journal of Plasticity* **116** 232–264
[24] Kimiecik M, Wayne Jones J and Daly S 2015 *Acta Materialia*
[25] Ren X, Miura N, Zhang J, Otsuka K, Tanaka K, Koiwa M, Suzuki T, Chumlyakov Y I and Asai M 2001 *Materials Science and Engineering A* **312** 196–206
[26] Gonzàlez-Comas A and Mañosa L 1996 *Physical Review B - Condensed Matter and Materials Physics* **54** 6007–6010
[27] Ding X, Zhang J, Wang Y, Zhou Y, Suzuki T, Sun J, Otsuka K and Ren X 2008 *Physical Review B* **77** 174103
[28] Rubinstein R Y and Kroese D P 2004 *The Cross-Entropy Method* (Springer New York)
[29] Marc - advanced nonlinear simulation solution `https://www.mscsoftware.com/product/marc` accessed: 2019-11-28
[30] *MSC Marc 2017, User Documentation, Volume B: Element Library*
[31] *MSC Marc 2017, User Documentation, Volume C: Program Input*
[32] *MSC Marc 2017, User Documentation, Python Tutorial and Reference Manual*
[33] Hill R 1952 *Proceedings of the Physical Society. Section A* **65** 349–354 ISSN 0370-1298
[34] Kröner E 1977 *Journal of the Mechanics and Physics of Solids* **25** 137–155 ISSN 0022-5096